Quantum Carrier Reinvestment-Induced Ultrahigh and Broadband Photocurrent Responses in Graphene–Silicon Junctions

Fangze Liu and Swastik Kar*

Department of Physics, Northeastern University, Boston, Massachusetts 02115, United States

ABSTRACT In an earlier work, we had reported a method that enables graphene–silicon junctions to display exceptionally high *photovoltaic* responses, exceeding 10^7 V/W. Using a completely different method that has recently been reported to result in ultrahigh gain, we now show that these junctions can also demonstrate giant *photocurrent* responsivities that can approach $\sim 10^7$ A/W. Together, these mechanisms enable graphene–silicon junctions to be a dual-mode, broad-band, scalable, CMOS-compatible, and tunable photodetector that can operate either in photovoltage or photocurrent modes with ultrahigh responsivity values. We present detailed validation of the underlying mechanism (which we call Quantum Carrier Reinvestment, or QCR) in graphene–silicon junctions. In addition to ultrasensitive photodetection, we present QCR photocurrent spectroscopy as a tool for investigating spectral recombination dynamics at extremely low incident powers, a topic of significant importance for optoelectronic applications. We show that such spectroscopic studies can also provide a direct measure of photon energy values associated with various allowed optical transitions in silicon, again an extremely useful technique that can in principle be extended to characterize electronic levels in arbitrary semiconductors or nanomaterials. We further show the significant impact that underlying substrates can have on photocurrents, using QCR-photocurrent mapping. Contrary to expectations, QCR-photocurrents in graphene on insulating SiO_2 substrates can be much higher than its intrinsic photocurrents, and even larger than QCR-photocurrents obtained in graphene overlaying semiconducting or metallic substrates. These results showcase the vital role of substrates in photocurrent measurements in graphene or potentially in other similar materials which have relatively high carrier mobility values.

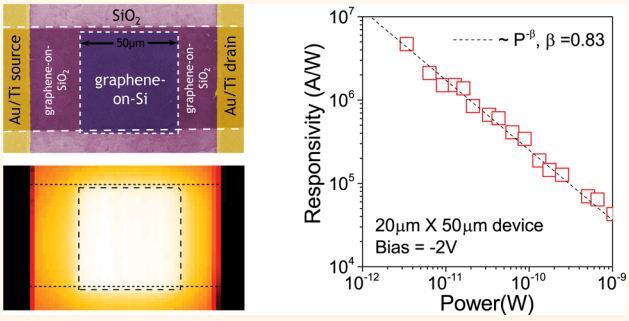

KEYWORDS: graphene · photodetector · quantum gain · carrier dynamics · optical transitions

Over the past decade, graphene has presented itself as an atomically thin material with extremely exciting electronic, photonic and optoelectronic properties.[1−4] To harness the attractive attributes of graphene into existing silicon-based platforms, there has been a growing effort in developing high-performance applications using graphene–silicon junctions. Examples of such applications include solar cells,[5] the "barristor",[6] optical modulators,[7] four-wave mixers,[8] Schottky diodes,[9] photodetectors,[10−13] gas sensors,[14,15] and electrodes for photoelectrochemistry.[16] The availability of large-area CVD-grown graphene[17,18] and high-quality wafer-scale transferring techniques[19] have extremely favorable implications for scalability and CMOS compatibility, and hence, technologies based on the graphene–silicon heterojunctions are very likely to receive increasing attention.

A number of the above-mentioned applications of graphene–silicon junctions involve the use of photons. Even those that do not could be subject to weak ambient lights. In our previous work,[11] we had shown that graphene–silicon interfaces tend to form Schottky-barrier like junctions, and the absorption of light by silicon can lead to injection of carriers into graphene, leading to sizable photovoltage differences between graphene and silicon ($V \rightarrow$ hundreds of millivolts). A fundamental question of considerable importance is how the injection of photoinduced carriers from silicon to

* Address correspondence to s.kar@neu.edu.

Received for review June 26, 2014 and accepted October 3, 2014.

Published online October 03, 2014
10.1021/nn503484s

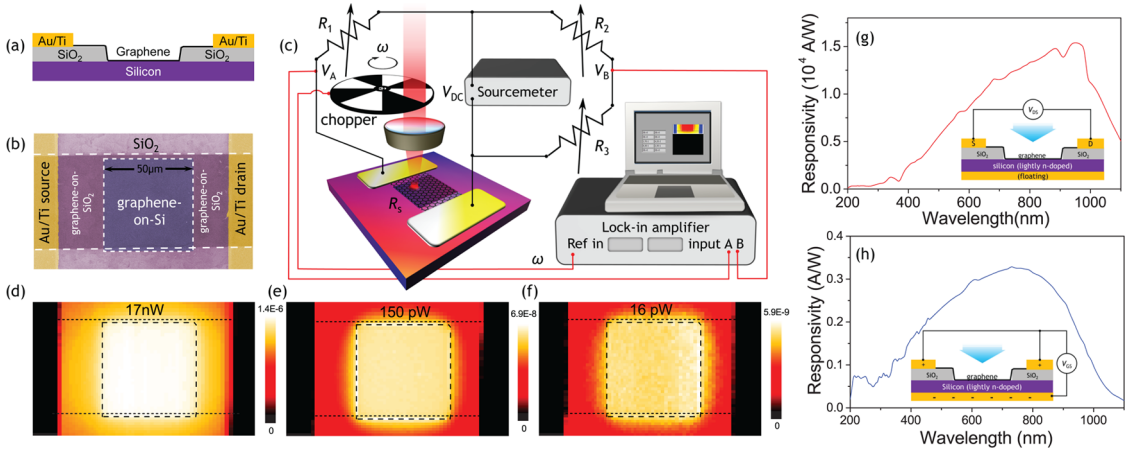

Figure 1. (a) A schematic and (b) a pseudo-colored SEM image of a graphene−silicon high-gain photodetector (see text). (c) A Wheatstone bridge-integrated, chopped-incidence scanning photocurrent microscopy and spectroscopy setup used to characterize the devices. (d−f) Typical photocurrent maps at different incident powers showing brightest photocurrent signal in the graphene−silicon region (color scale in amperes). Spectral responsivity in the same device in (g) high-gain mode and (h) photodiode mode. Note the spectacular difference in their magnitudes, even though the spectral shapes are similar.

graphene can affect the electronic properties of the latter. Given the growing importance of these junctions, it is imperative that nature of carrier dynamics across these junctions are carefully investigated.

In this work, we look critically at the effect that photoinduced carrier injection has on the electrical properties of graphene. On the basis of recent works by Konstantatos *et al.*[20] and Roy *et al.*,[21] we lay down a simple model for the carrier injection and recombination process, and how this results in excess photocurrents in graphene. We then use this model to predict and experimentally verify the photocurrent change as a function of the applied drain-source bias across graphene (V_{DS}), the size (L) of the devices, and the recombination time scale. The recombination time scale is a critical parameter in this system, and we find that this could vary significantly, over 2 orders of magnitude as a function of incident light power, reaching values exceeding a millisecond at the lowest tested powers. The large recombination time scale and the ultrafast transition of carriers within graphene render the injected carriers ultrahigh quantum gain values that exceed 10^6 electrons per incident photon, resulting in these junctions being highly efficient photodetectors with responsivities that approach $\sim 10^7$ A/W. We also present detailed spectral response of photocurrents generated through this mechanism, a method that allows us to directly obtain recombination time scales as a function of photon energy under very low-intensity incidences, as well as identify various allowed interband optical transitions in silicon. Further, as a result of this ultrahigh gain mechanism, photocurrent response in graphene is sensitive to charge-injection from any surface, and we demonstrate how this feature can be made use of to clearly distinguish between metallic, semiconducting and insulating underlying layers in the same device. On one hand, this result could be viewed as an interesting new method by which the carrier injection dynamics of underlying layers may be directly imaged. On the other hand, it clearly shows that the accurate measurement of photocurrents in graphene-based devices needs very careful consideration of carriers injected from the underlying substrates.

RESULTS AND DISCUSSION

Figure 1 outlines the basic device architecture and measurement technique used to characterize the graphene−silicon junctions. Figure 1a shows a cross-sectional schematic of the most commonly used device configuration (high-gain mode). It comprises a sheet of graphene, the central part of which is physically overlaid on top of a bare silicon surface, and the ends are placed on a layer of insulating SiO_2 where they are attached to external electrodes. During the experiment, light is incident on the graphene−silicon junction area. Figure 1b is a pseudo-colored SEM image of a typical device, where the (largely) monolayer, CVD-grown[17] graphene sheet was first mechanically transferred, and then lithographically etched to approximately match the width of the silicon window. The silicon window was fabricated by etching out a 100 nm thick oxide layer and graphene was transferred onto this surface immediately. At various regions, the graphene sheet lies over silicon and SiO_2 areas; these and metal contact regions are shown (see details in Supporting Information) Figure 1c schematically shows the bridge-based circuit configuration used for low-noise, a/c detection of photocurrents. The bridge was balanced in complete darkness, and the chopper frequency ($\omega/2\pi$) was used as a reference for a lock-in amplifier. Three low-noise variable resistors were adjusted to be as close to the sample (dark) resistance as possible, to obtain equal dark current in both arms

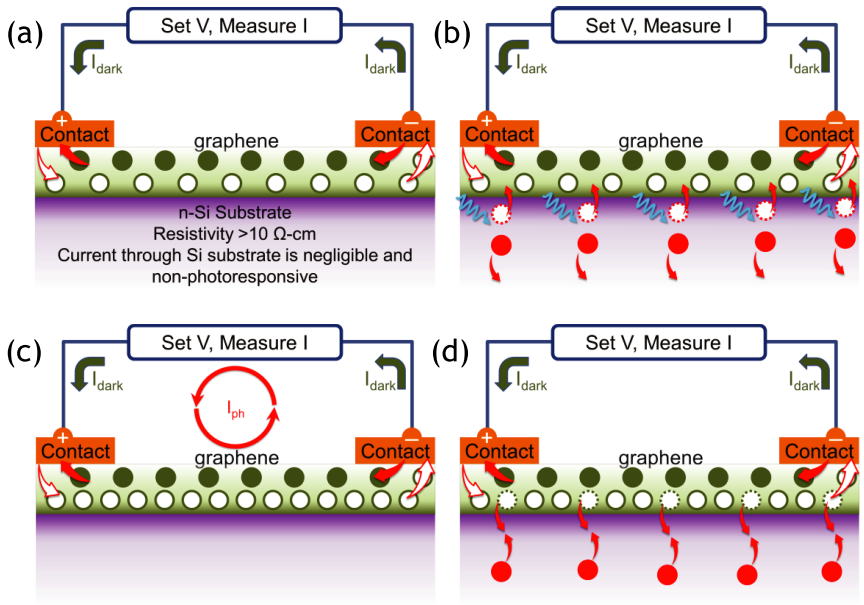

Figure 2. Schematics outlining the gain mechanism at graphene–Si junctions. (a) Dark current (I_{dark}) under an external bias (V) due to intrinsic carriers in graphene. Electrons and holes are denoted by dark and light circles, respectively. (b) Incident photons generate electron–hole pairs in the (lightly n-doped) silicon. Due to the built-in potential at the junction (see Figure 3c), holes inject out into graphene, while electrons move away from the junction as indicated by the arrows. (c) These injected carriers "dope" graphene and remain available for a certain time-scale, τ_r, before they recombine back into silicon. During this time, the applied bias V replaces these carriers several times by driving them through the external circuit, causing the photocurrent, I_{ph}, as shown. (d) At the end of their lifetime, these carriers recombine back into silicon. Since graphene possesses ultrafast carrier transport with high mobility, a single photoinduced extra carrier may be recirculated several times during its lifetime, effectively leading to a quantum gain.

and maximum sensitivity. The sample was mounted on a computer-controlled $X-Y$ stage with submicrometer precision. The spot size was focused by a 100× lens to about a micrometer for photocurrent mapping measurements. The a/c bridge configuration allowed us to directly measure the RMS of the first harmonic response (ω) of the total photocurrent I_{ph} ($I_{ph} = V_{AB}/R_s$), which we estimated to be about 45% of the DC response($\sqrt{2}/\pi$, assuming the input, V_{AB}, is a square wave). In experiments where the response of the entire device was being tested, the light was made to cover the entire junction area, and for experiments involving measurements of response time-scale and reproducibility, the lock-in amplifier was replaced by an oscilloscope in order to capture the transient responses.

Figure 1d–f shows the photocurrent map of the device shown in Figure 1b measured using light spots focused from a $\lambda = 633$ nm laser using a fixed DC bias, $V_{DC} = 1$ V (*i.e.*, $V_{DS} = 0.5$ V across the device), and with different incident powers (P) as shown. The maximum photoresponse is seen in the graphene–silicon window region, which immediately suggests that the carriers generating the photocurrents are originated from silicon, and are not intrinsic photoexcited carriers in graphene. The role of silicon can be further confirmed by investigating the spectral dependence of photocurrent response. With the use of a variable wavelength monochromated light source, it was possible to study the spectral response at a fixed incident power. Figure 1g shows the spectral photocurrent response in a device, measured in the high-gain mode (see inset). A rather large photocurrent responsivity, $R(\lambda) = I_{ph}(\lambda)/P(\lambda)$ of the order of 10^4 A/W is seen in this device. We recall that due to its low absorption coefficient of about 2.3%, intrinsic photocurrent in graphene is limited to a few milliamperes per watts (mA/W).[22–24] Since the photocurrent responsivities seen in these devices are many orders of magnitude larger, as seen in Figure 1g, we conclude that the photocurrent measured in these samples had insignificant contributions from photocarriers generated in graphene. At the same time, the spectral shape of the responsivity curve in Figure 1g is similar to that of Figure 1f, where the responsivity has been measured in the photodiode mode,[11] clearly indicating that most of the photoinduced carriers originate in silicon and then get injected into graphene. It is interesting to note how far more efficient the photon-to-carrier conversion is in the high-gain mode (Figure 1g) compared to the photodiode mode (Figure 1h), resulting in the orders-of-magnitude higher responsivity in the former. In the remaining portion of this work, we investigate this phenomenon in greater detail.

The photoinduced injection of carriers into graphene can be understood through a simple model (originally proposed by Konstantatos *et al.*[20]) as outlined in Figure 2. Consider a junction between graphene and lightly n-doped silicon. The light n-doping

helps us fix the location of the Fermi level of silicon just below its conduction band, even though silicon remains highly nonconductive (compared to graphene). Under an applied external bias V_{DS}, and in darkness, a dark current I_{dark} flows through the external circuit due to the intrinsic carriers in graphene, as shown in Figure 2a. When illuminated, electron−hole pairs are generated in silicon. Due the nature of the Schottky-type barrier formed at the junction,[11] the electrons move away into the body of silicon, and holes get injected across the junction into graphene, as shown in Figure 2b. These additional holes that inject into graphene result in a change of sheet current (=I_{ph}, Figure 2c), arising from the "borrowed" holes from silicon. Under the applied external bias, the "borrowed" additional carrier may be removed from its quantum mechanical state (through an external metal lead on one side of graphene), and the empty state may be subsequently replaced by another carrier (injected in from a second lead on the other side), generating an electrical current in an external circuit. Due to the extremely rapid transit of carriers within graphene, a single borrowed carrier can be replaced many times before another "equivalent" hole reverse-injects across the junction into silicon (Figure 2d). During the lifetime of the "borrowed" carrier, τ_r, a time scale determined by the quantum-mechanical probability of recombination, the borrowed carrier can be "reinvested" several times into the external circuit, adding to the net photocurrent, and leading to a quantum gain. For convenience, we call it the quantum carrier reinvestment (QCR) mechanism, to distinguish it from photogating,[25] photodoping,[26] photovoltaic[11] or photoconductive[27] effects.

The QCR mechanism in graphene-based hybrid structures has been successfully implemented very recently by two groups, to obtain ultrasensitive photodetectors[20] using graphene−quantum dot hybrid structures, and novel photomemory devices,[21] using graphene−MoS_2 heterojunctions. The key factor that drives the gain mechanism in QCR is the interplay of two time scales. Due to the ultrafast recombination time scale of picoseconds in graphene,[28] photoexcited carriers recombine well before they can be circulated out into an external circuit. As a result, it is quite difficult to obtain intrinsic photoconductive gain in graphene. In contrast, if the photoexcited carriers are "borrowed" from a neighboring material across a junction with a favorable built-in potential drop, these carriers can survive much longer than intrinsically photoexcited carriers within graphene. Further, if the intrinsic recombination time scale of the secondary material is slow, it can further reduce the recombination rate. We next try to obtain a model that relates the quantum gain with these time scales.

We start by defining the external quantum efficiency (QE) as the number of carriers created in silicon and then injected across the graphene−silicon junction per incident photon. This number is typically between 50% and 65% in most of the visible wavelengths in graphene−silicon junctions.[11] The number of times that each injected carrier is "reinvested" is equal to the ratio of the recombination time, τ_r, to the electrode-to-electrode transit time, τ_t. The quantum gain, QG, can then be related to the quantum efficiency through this ratio, *i.e.*, $QG = QE \times (\tau_r/\tau_t)$. Assuming free-electron-type transport in graphene, τ_r is related to the drift velocity, $\tau_t^{-1} = v_d/L = \mu \times E/L$, where μ is the mobility of graphene, E is the applied electric field (=V/L), and L = length between the electrical contacts, which implies $QG = QE \times \tau_r \times \mu V/L^2$. For incident light of wavelength λ, and incident power P, photocurrent responsivity is given by $R = I_{ph}/P = (e\lambda/hc) \times QG = (e\lambda/hc) \times QE \times \tau_r \times \mu V/L^2$. This expression implies that the photocurrent response should be linearly dependent on the applied drain-source bias, inversely proportional to the square of the device size, and directly proportional to the recombination time scale of the system. We next present results from a set of experiments designed to investigate these predictions.

Figure 3 summarizes a range of experiments we have performed to establish the efficacy of the QCR model for a whole range of devices tested for a variety of experimental conditions. Figure 3a shows a simplified schematic of the different measurement configurations tested. In addition to the drain and source electrodes that were used to apply an external bias across the graphene sheet V_{DS}, a separate ohmic contact was fabricated on the back-surface of the silicon wafer. When a DC voltage is applied across the graphene−silicon junction, V_{GS} tunes the potential difference on the two sides of the junction, effectively allowing us to play around with the recombination time scale. The data presented here is for lightly n-doped silicon, with a doping level $n \leq 10^{16}$ cm^{-3} and resistivity $\rho \geq 10\ \Omega\cdot$cm. We have also tested p-doped silicon devices with equal success (see p-doped Si in Supporting Information). The photocurrent response of bare silicon devices were separately tested and found to be negligible. Figure 3b shows the transient photocurrent response as monochromatic light was chopped on and off, showing immediate response and reproducibility of the photocurrent (see Figure S6 in Supporting Information for stability and repeatability test for extended time scale). Figure 3c shows a proposed energy-level diagram of the graphene−silicon junction, including how the Fermi levels line-up on both sides, giving rise to a Schottky-like barrier. Incident photons create e−h pairs, and in this case, holes get injected into graphene across the junction, lowering the Fermi level to its new position, *i.e.*, the quasi Fermi level.[11] This lowering explains why the photocurrent observed in Figure 3b is negative.

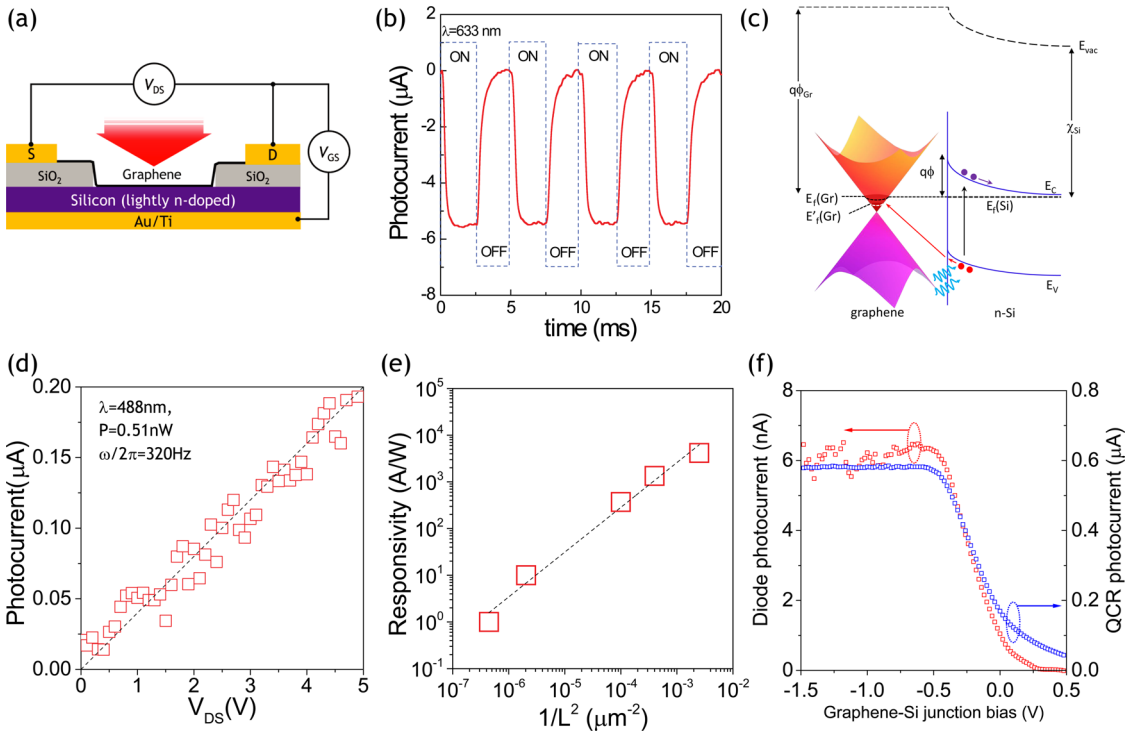

Figure 3. (a) Device configuration for testing the QCR model (see text). Lightly n-doped silicon was used to fix the Fermi level below the conduction band. (b) Time-dependent response to the periodic chopping of light source, demonstrating the reproducibility of the photodetection. (c) Schematic band-alignment diagram of the graphene–Si junction explaining the generation and movement of electrons and holes under the formation of a Schottky-type barrier. (d) Photocurrent as a function of V_{DS} for a device of L = 100 μm under 0.51 nW illumination. (e) Variation of responsivity as a function of $1/L^2$, where L is the device length. (f) Variation of QCR and diode-mode photocurrent as a function of an applied graphene–silicon junction bias, V_{GS}.

To test the linearity of the photocurrent with the applied source-drain bias, V_{DS}, the graphene–silicon junction voltage, V_{GS} was kept open (floating). Figure 3d shows the photocurrent response as a function of applied source-drain bias, which is seen to remain linear over the entire voltage range tested. The linear bias dependence of the photocurrent is a very important result, as it implies that the photoresponsivity of these devices can be completely tuned, to obtain a responsivity of choice, a very important feature for developing tunable photodetectors, and for imaging applications that can adjust to variable lighting conditions. A more stringent examination of the QCR mechanism comes from examining its applicability over devices of different sizes. Figure 3e shows the variation of responsivity as a function of device size. In each case, the error in estimation of responsivity is smaller than the size of the data points shown. We find that over several orders of magnitude change in device length L ($1/L^2$ ranges over 4 orders of magnitude), the responsivity remains linearly dependent on $1/L^2$ within experimental error. We note here that this not only provides strong evidence of the validity of this model, but also reflects on the highly reproducible nature of QCR in devices that range from tens of micrometers to several millimeters in dimension.

Figure 3f shows the variation of the QCR photocurrent and diode photocurrent from the same device as a function of the graphene–silicon junction bias. On one hand, applying a reverse bias shifts the Fermi level of graphene (E_f(Gr)) upward,[29] implying that the re-entry barrier for holes (from graphene to silicon) is higher. The photocurrent is enhanced as a result of longer recombination time scale. On the other hand, application of a forward bias lowers its Fermi level and brings it closer to the valence band of silicon. This effectively lowers the barrier for holes to reverse-inject into silicon and recombine with available electrons. At the same time, under forward bias, electrons are not "pushed away" from the graphene–silicon junction. These two factors combined can significantly decrease the lifetime of the injected carriers, which would then result in a smaller photocurrent. At a "threshold" forward bias which is close to the size of the Schottky barrier ($V_{GS} \simeq$ 0.5 V, see Supporting Information), the re-entry barrier will be so low that the probability of holes injecting in and out of graphene will be equal, resulting in a vanishing photocurrent. Since the diode photocurrent directly reflects how many holes were injected into graphene, both QCR and diode photocurrent should behave the same as a function of bias voltage, shown in Figure 3f. Again, this provides an independent method for completely tuning the photocurrent responsivity of the devices. (Band diagrams and photocurrent under different incident power are in Supporting Information.)

Having demonstrated that the high-gain response in graphene–silicon junctions indeed follow the QCR

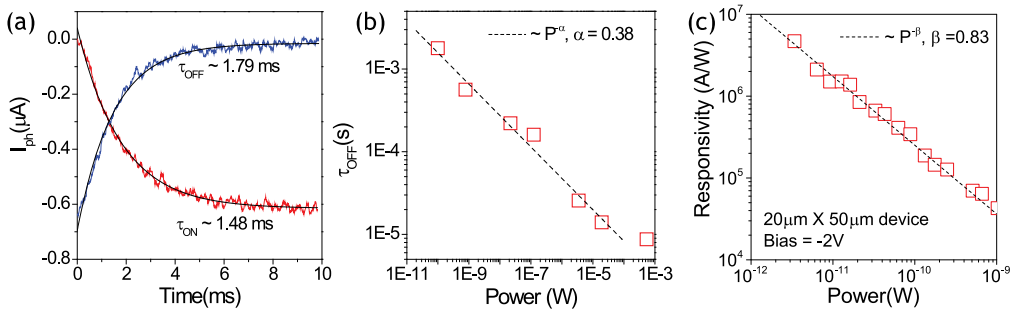

Figure 4. (a) Temporal response at chopping frequency of 50 Hz and 488 nm laser power of 0.1 nW; τ_{ON} and τ_{OFF} are calculated by exponential fitting. (b) Variation of τ_{OFF} as a function of several decades of incident power. (c) Variation of responsivity as a function of incident power. According to the trend seen here, the responsivity exceeds 10^6 A/W and approaches 10^7 A/W as the incident power approaches picowatts.

model, we next examine a number of other important features of photodetection in graphene−silicon junctions in this mode. Figure 4a shows the time-dependence of photoresponse in a typical device as the incident light is chopped on or off. The time-scale of chopping is much smaller (of the order of 20 μs). A response-time of the order of milliseconds is seen for incident light power of ~0.1 nW. The millisecond switching response implies that arrays of such photodetectors would be ideally suitable for the development of imaging, videography, or time-resolved spectroscopy applications, without the need for any reseting mechanism. Moreover, we find that the switching times are strongly dependent on the incident light power.

Figure 4b shows the variation of τ_{OFF} as a function of incident power, which is seen to rise sharply as a function of decreasing incident light power. We recall that the quantum gain (and hence the photocurrent responsivity) is linearly dependent on the recombination time-scale, τ_r. Since the recombination processes are statistically random, we assume that the system is Ergodic (time average ≡ ensemble average), *i.e.*, the recombination time-scale τ_r is the same as τ_{OFF}. Since τ_{OFF} rises sharply as the incident light-power is decreased, the responsivity, which is directly proportional to τ_{OFF}, is also expected to increase. Figure 4c shows the variation of responsivity as a function of incident light power. Indeed, we find a sharp power-law rise of responsivity as the incident light intensity is decreased, and this behavior is seen to retain its consistency over several decades of incident power values. At the lowest measured incident powers (as the incident power approaches picowatts), the responsivity exceeds a few 10^6 A/W and approaches 10^7 A/W, corresponding to quantum gain factors of 10^6−10^7. We do note, however, that the rise in responsivity as a function of decreasing incident powers is almost twice as sharp as compared to that of τ_{OFF}. This is most likely because of capacitor-like Coulomb-repulsion effects at higher incident powers that increasingly suppresses carrier injection into graphene as the excess charge density on graphene grows. Nevertheless, such ultrahigh photocurrent responsivity and quantum gain in such low-voltage devices is extremely attractive for low-intensity measurements where high responses are greatly desirable. These results are comparable to those of other graphene-based junctions that have used QCR to develop photodetectors and memory devices.[20,21] Moreover, by using silicon as the light-absorbing material along with CVD-grown graphene, our devices remain operational in the broadband visible wavelength range, and furthermore are completely compatible with CMOS-integrable silicon photonics platforms. We now move on to discuss two other applications beyond photodetection that arise as a direct consequence of the QCR mechanism.

A predictable outcome of the QCR mechanism is that its resulting spectral dependence of photoresponse is determined by the underlying material, in this case silicon. Indeed, this fact is directly responsible for the approximately similar spectral shapes of responsivities seen in Figure 1g,h. We find that beyond this obvious similarities of spectral shapes, these measurements contain other interesting information. We recall that the responsivity measured in the photodiode mode is a direct measure of the external quantum efficiency[11] through the relation, $R(\lambda) = (e\lambda/hc) \times$ QG. The quantum efficiency is a direct measure of how many carriers get injected across the junction and out into graphene (per incident photon) in the absence of any gain mechanism. Hence, when we measure the responsivity in photodiode and QCR modes in the same device, it is possible to obtain the QCR gain factor, QG/QE. Figure 5a shows the QCR gain factor, QG/QE = (τ_r/τ_t) as a function of photon energy. This was measured on the same device investigated in Figure 4a, under similar incident powers over the entire spectrum. Using $\tau_{OFF} = \tau_r = 1.79$ ms at $\lambda = 488$ nm (E_{ph} = 2.54 eV), we obtain $\tau_t \approx 10^{-7}$ s. At an applied bias of 0.25 V for an L = 100 μm device, this corresponds to a mobility of ~4000 $cm^2/(V \cdot s)$, which is similar to the field-effect mobility of high-quality CVD-grown graphene.[17,31,32] Moreover, since τ_t is an intrinsic property of graphene, depending only on its mobility, it is

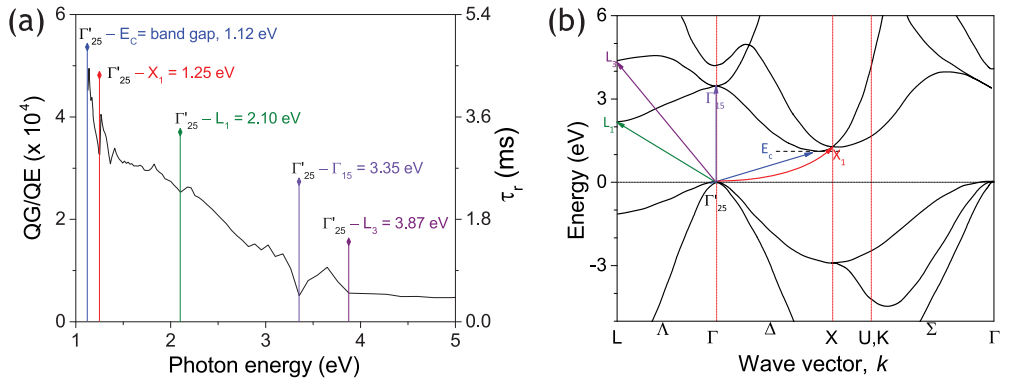

Figure 5. QCR spectroscopy as a direct measure of recombination time scales in graphene–silicon junction. (a) Spectral dependence of the QCR gain factor, QG/QE, as well as the extrapolated recombination time (τ_r). Some spikes in the data could be associated with various optical transitions in silicon as outlined in the schematic electronic structure shown in (b) (adapted with permission from ref 30; copyright 1974 American Physical Society).

safe to assume that τ_t will remain independent of incident photon energy values. Hence, it is possible to directly obtain the extrapolated value of τ_r *vs* photon energy from the QCR gain-factor spectrum, without actually measuring it. The right-axis of Figure 5a also shows the corresponding values of the recombination time scale τ_r. We note that this method of direct lock-in based measurement of τ_r is extremely useful at very low light incidences, when DC transient responses become comparable to instrument noise-levels. As we show later, this provides us a new way for directly comparing the surface charge dynamics in materials with different injection time scales under varying incident light powers.

The spectral dependence of QCR gain factor provides a wealth of information regarding the electronic structure of underlying semiconductor. As seen in Figure 5a, the gain factor has an overall slow decrease with increasing photon energy values, and this slow decrease in recombination time scales may be related to gradually increasing tunneling-induced recombination events in carriers that receive higher excitation energy values. Riding on this slow change are several spectral features in the form of sudden "jumps" or sharp changes in the QCR gain factor. The origin of these peak-like features can be directly traced to the energy related to a number of possible electronic transitions in silicon. To elucidate this point, we have drawn a schematic band structure of silicon in Figure 5b (adapted with permission from Chelikowsky *et al.*[30]), with some of the relevant critical points as labeled. When we compare panels a and b in Figure 5, several optical transitions are immediately identifiable. Starting at the indirect band gap, corresponding to transitions between the maximum of the valence band at the Γ-point, Γ'_{25}, to the next-higher energy-minimum along the $\Gamma \rightarrow X$ symmetry direction (Δ), the QCR gain factor curve shows multiple identifiable transitions corresponding to $\Gamma'_{25} \rightarrow X_1 \approx 1.25$ eV, $\Gamma'_{25} \rightarrow L_1 \approx 2.1$ eV, $\Gamma'_{25} \rightarrow \Gamma_{15} \approx 3.35$ eV, and $\Gamma'_{25} \rightarrow L_3 \approx 3.87$ eV. These transitions, annotated by labels of specific colors in Figure 5a, are denoted by arrows of corresponding colors in Figure 5b. In addition to these identifiable transitions, a number of other features are also present, but could not be immediately associated with the electronic structure of silicon. These approximately few electronvolt transitions are most probably related to excitations from dopant and impurity levels. Hence, we find that the QCR mechanism is extremely useful for performing ultralow light spectroscopic investigation of carrier time scales, which is extremely important for many photonic and photovoltaic applications, and can vary significantly with incident powers, as seen in Figure 4b. Moreover, the same technique gives us a novel way of identifying interband optical transitions in silicon, and can potentially be applied to other semiconductors and nanomaterials that form heterojunctions with graphene.

Finally, we explore another very important aspect of the QCR mechanism, the role of substrates on photoresponse in graphene. Due to the enormous gain factors involved, charges injected into graphene from neighboring materials can result in photocurrents which are orders of magnitude larger than intrinsic photoexcited response in graphene. To investigate this, we have constructed a device where the same graphene sheet overlays three electronically different types of materials, (a) metal, (b) semiconductor, and (c) insulator, as shown in Figure 6a. This was accomplished by lithographically fabricating an array of silicon islands (lateral size 15 μm × 15 μm, height 50 nm) on a 400-nanometer-thick insulating SiO_2 surface. Au electrodes were fabricated on two ends, and a sheet of graphene was transferred on top of this composite array of multimaterial substrate. Figure 6b shows a pseudo-colored SEM image of this device, where the different regions (metal, semiconductor, and insulator) have been demarcated by arrows. A fixed voltage was applied across the two metal electrodes. Figure 6c–e shows photocurrent maps measured on these devices

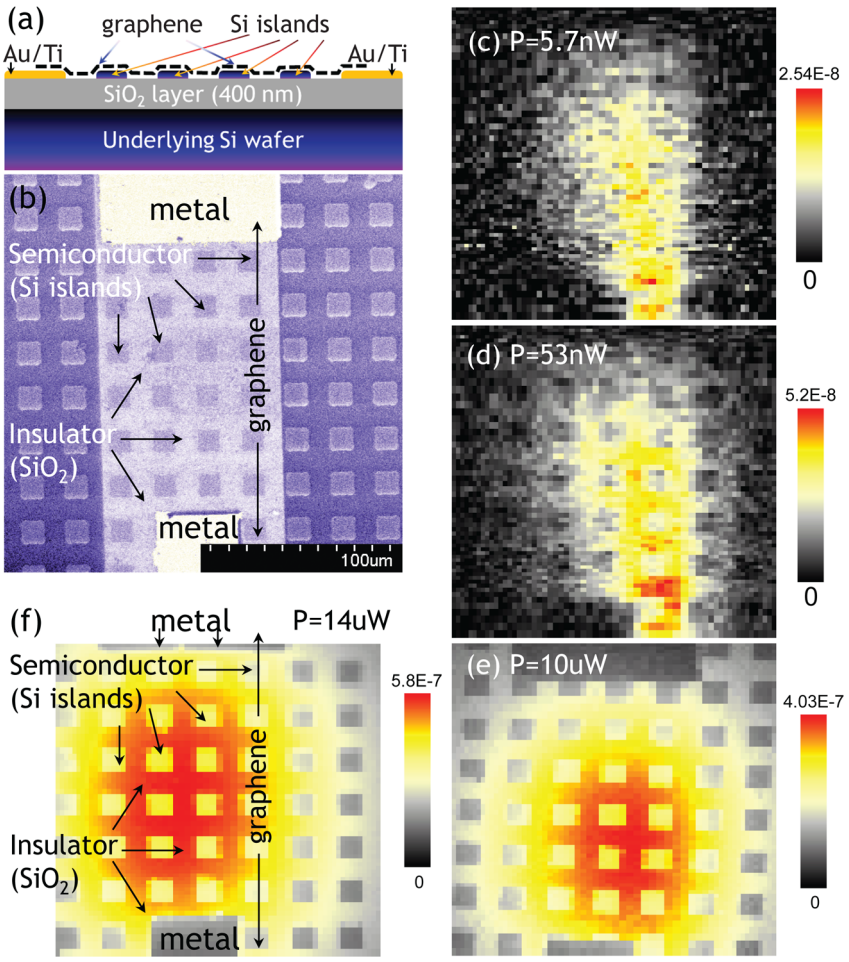

Figure 6. (a) A schematic and (b) a pseudo-colored SEM image of a patterned, multisubstrate device designed to investigate the effect of substrates on photocurrent response due to the QCR mechanism. The metallic, semiconducting, and insulating regions, and the overlaying graphene sheet are indicated by arrows. (c–e) The photocurrent map was measured on this device using a 488 nm incident light chopped at 100 Hz. The bias across the device is 2.5 V, and the incident power was varied as indicated. As the incident power increases, the photocurrent response due to QCR from different substrates gets increasingly distinct. (f) Photocurrent map at the highest measured incident power, P = 14 μW, and the different substrate regions are clearly indicated. In all the maps, the color-scalebar is in amperes.

at different incident powers. At the lowest incident power, the local responsivity (R_{spot}) ranged between 2 and 4 A/W implying that the photocurrent is not due to intrinsic carriers in graphene.

At this power-level, the photocurrent map is diffused, varying slowly across the device, but indicating no distinction between different substrate regions. This implies that the quantity QE $\times$ τ_r is similar for junctions formed at different regions. However, as the incident power is gradually increased, the photocurrent response from different regions become increasingly distinguishable, with clear patterns (correlated with the geometry of the silicon islands and metal electrodes) emerging, as seen in Figures 6d,e. This is not surprising, since both quantum efficiency and the recombination time scales can be expected to change differently in different materials as the incident power increases, providing a interesting method for "imaging" graphene subsurface materials. Figure 6f shows the photocurrent map at P = 14 μW, where the underlying features are well-formed, and the various "types" of materials below the graphene sheet indicated by arrows. These maps bring out several extremely important features of graphene-based photocurrent measurements. First, contrary to our expectations, it is the "insulating" SiO_2 regions which demonstrate the highest photocurrent responses. One would expect that insulating regions, with little or no carriers would provide very few photoinduced carriers under incident light, and hence photoresponse coming from these surfaces are expected to be quite low. However, it turns out that the carriers, which are most likely excited from defects and trap states in the oxide, have extremely long lifetimes (minutes to hours[33]) and hence result in high QCR gain factors. In contrast, although the silicon islands have more carriers to offer, the recombination time scales are faster and this compensates the overall photoresponse, generating intermediate values of photocurrents. The extreme opposite situation occurs at metal–graphene junctions

(at the electrodes). Metals have very high number of carriers to offer, but the recombination from graphene to metals can be of the order of picoseconds, resulting in little or no photocurrent response at these regions (in comparison to the semiconducting and insulating regions). These experiments clearly indicate that substrate- or top-gate related effects are extremely important to consider when performing photocurrent-based experiments in graphene. This is specifically so for SiO_2, which is one of the most commonly used substrates, and can have a very significant impact on these measurements.

CONCLUSIONS

In conclusion, we have presented a detailed investigation of high-gain photoresponse at graphene−silicon junctions. We refer to the underlying photoresponse mechanism as quantum carrier reinvestment due to the manner in which photocarriers are borrowed into graphene and reinvested several times in the external circuit during its lifetime, resulting in a quantum gain. Due to the significantly high mobility values of graphene, the quantum gain factors can exceed 10^6, resulting in these junctions becoming ultrasensitive weak-incidence broadband photocurrent detectors with photocurrent responsivity values nearly approaching 10^7 A/W at approximately picowatt incidences. We note that this mechanism complements the photovoltage-based detection at the similar junctions, which utilizes the unique band-structure of graphene (and not its mobility) to result in ultrasensitive photovoltage detectors with photovoltage responsivity exceeding 10^7 V/W. Together, these two completely independent mechanisms can result in graphene−silicon junctions to be utilized as tunable dual-mode (either in photocurrent or in photovoltage mode) broadband, visible wavelength photodetectors with ultrahigh responsivities under weak illuminations. We have utilized a free-electron-theory type model to elucidate the role of applied bias and device size, as well as recombination time scales on the photoresponse behavior at these junctions. We have also shown how the spectral dependence of these recombination time scales at very weak incidences can be directly obtained from lock-in amplifier-based photocurrent measurements. These spectra have features directly related to transitions within various energy levels in silicon, providing an interesting new method for direct investigation of possible optical transitions in semiconductors. Further, we have investigated the importance of substrates in photocurrent measurements of graphene, and established that SiO_2, one of the most commonly used substrates, can have the maximum impact on photocurrent measurements in graphene. This can be a matter of concern in many graphene (or any other high-mobility 2D material)-based optoelectronic experiments where the role of substrates, gate-oxides, *etc.* is not carefully taken into consideration. Using a power-dependent photocurrent mapping technique, we have also presented a new method that can compare the carrier dynamics across graphene-based junctions of different materials. This technique may provide a new way for understanding variations of carrier dynamics across such junctions with micrometer spatial resolution. Such measurements could be of great interest to obtain optimized performances in a number of optoelectronic devices that use graphene-based junctions. We believe our work is a significant step forward in the optoelectronics of graphene-based junctions, especially in characterizing carrier time scales that are applicable to diverse semiconductors and nanomaterials that can form junctions with graphene. Indeed, a generic understanding of the QCR mechanism is highly important, since it can, in principle, affect the photoresponse in junctions of any nanomaterial (and not just graphene) which has comparatively high mobility values.

METHODS

Synthesis of Graphene. Graphene was grown by CVD method. Twenty-five micrometers copper (Cu) foil was first annealed at 1000 °C in a tube furnace with a hydrogen flow of 10 sccm for 30 min. Then a 30 min methane flow of 5 sccm was used for growth while keeping the same hydrogen flow rate. After the growth, the furnace was cooled down naturally at a rate of ~30 °C/min. To transfer graphene, the graphene−Cu foil was spin-coated with poly(methyl methacrylate) (PMMA) in order to protect and support the graphene sheet while the Cu foil was etched away in diluted nitric acid. PMMA was removed in acetone after the transfer process. See detailed characterizations of graphene and device fabrication procedures in Supporting Information.

Characterization. SEM images were taken with a Hitachi S-4800. All DC signals were collected by a Keithley 2400 sourcemeter, and AC signals by a Stanford Research Systems SR830 lock-in amplifier. Spectral responsivity tests were carried out inside a PerkinElmer UV/vis spectrophotometer using the AC-bridge configuration.

Conflict of Interest: The authors declare no competing financial interest.

Acknowledgment. The authors gratefully acknowledge financial support provided by the National Science Foundation, Grant Number ECCS 1351424, and a Northeastern University Provost's interdisciplinary Tier-1 seed grant.

Supporting Information Available: More details about graphene synthesis and device fabrication, characterizations of graphene/Si junctions, stability and reliability test and comments on the negative photocurrent. This material is available free of charge *via* the Internet at http://pubs.acs.org.

REFERENCES AND NOTES

1. Castro Neto, A. H.; Guinea, F.; Peres, N. M. R.; Novoselov, K. S.; Geim, A. K. The Electronic Properties of Graphene. *Rev. Mod. Phys.* **2009**, *81*, 109–162.
2. Geim, A. K.; Novoselov, K. S. The Rise of Graphene. *Nat. Mater.* **2007**, *6*, 183–191.

3. Schwierz, F. Graphene Transistors. *Nat. Nanotechnol.* **2010**, *5*, 487–496.
4. Bonaccorso, F.; Sun, Z.; Hasan, T.; Ferrari, A. C. Graphene Photonics and Optoelectronics. *Nat. Photonics* **2010**, *4*, 611–622.
5. Won, R. Photovoltaics: Graphene–Silicon Solar Cells. *Nat. Photonics* **2010**, *4*, 411.
6. Yang, H.; Heo, J.; Park, S.; Song, H. J.; Seo, D. H.; Byun, K.-E.; Kim, P.; Yoo, I.; Chung, H.-J.; Kim, K. Graphene Barristor, a Triode Device with a Gate-Controlled Schottky Barrier. *Science* **2012**, *336*, 1140–1143.
7. Liu, M.; Yin, X.; Erick, U.; Geng, B.; Zentgraf, T.; Ju, L.; Wang, F.; Zhang, X. A Graphene-Based Broadband Optical Modulator. *Nature* **2011**, *474*, 64–67.
8. Gu, T.; Petrone, N.; F, M. J.; Zande, A.; Yu, M.; Lo, G.; Kwong, D.; Hone, J.; Wong, C. Regenerative Oscillation and Four-Wave Mixing in Graphene Optoelectronics. *Nat. Photonics* **2012**, *6*, 554–559.
9. Chen, C.-C.; Aykol, M.; Chang, C.-C.; Levi, A. F. J.; Cronin, S. B. Graphene-Silicon Schottky Diodes. *Nano Lett.* **2011**, *11*, 1863–1867.
10. Wang, X.; Cheng, Z.; Xu, K.; Tsang, H. K.; Xu, J. High-Responsivity Graphene/Silicon-Heterostructure Waveguide Photodetectors. *Nat. Photonics* **2013**, *7*, 888–891.
11. An, X.; Liu, F.; Jung, Y. J.; Kar, S. Tunable Graphene–Silicon Heterojunctions for Ultrasensitive Photodetection. *Nano Lett.* **2013**, *13*, 909–916.
12. Lv, P.; Zhang, X.; Zhang, X.; Deng, W.; Jie, J. High-Sensitivity and Fast-Response Graphene/Crystalline Silicon Schottky Junction-Based Near-IR Photodetectors. *IEEE Electron Device Lett.* **2013**, *34*, 1337–1339.
13. Fan, G.; Zhu, H.; Wang, K.; Wei, J.; Li, X.; Shu, Q.; Guo, N.; Wu, D. Graphene/Silicon Nanowire Schottky Junction for Enhanced Light Harvesting. *ACS Appl. Mater. Interfaces* **2011**, *3*, 721–725.
14. Singh, A.; Uddin, M. A.; Sudarshan, T.; Koley, G. Tunable Reverse-Biased Graphene/Silicon Heterojunction Schottky Diode Sensor. *Small* **2014**, *10*, 1555–1565.
15. Uddin, M. A.; Singh, A. K.; Sudarshan, T. S.; Koley, G. Functionalized Graphene/Silicon Chemi-Diode H_2 Sensor with Tunable Sensitivity. *Nanotechnology* **2014**, *25*, 125501.
16. Wu, K.; Quan, W.; Yu, H.; Zhao, H.; Chen, S. Graphene/Silicon Photoelectrode with High and Stable Photoelectrochemical Response in Aqueous Solution. *Appl. Surf. Sci.* **2011**, *257*, 7714–7718.
17. Li, X.; Cai, W.; Colombo, L.; Ruoff, R. S. Evolution of Graphene Growth on Ni and Cu by Carbon Isotope Labeling. *Nano Lett.* **2009**, *9*, 4268–4272.
18. Bae, S.; Kim, H.; Lee, Y.; Xu, X.; Park, J.-S.; Zheng, Y.; Balakrishnan, J.; Lei, T.; Kim, H. R.; Song, Y. I.; *et al.* Roll-to-Roll Production of 30-Inch Graphene Films for Transparent Electrodes. *Nat. Nanotechnol.* **2010**, *5*, 574–578.
19. Gao, L.; Ni, G.; Liu, Y.; Liu, B.; Neto, A. H. C.; Loh, K. P. Face-to-Face Transfer of Wafer-Scale Graphene Films. *Nature* **2014**, *505*, 190–194.
20. Konstantatos, G.; Badioli, M.; Gaudreau, L.; Osmond, J.; Bernechea, M.; Arquer, F. P. G. d.; Gatti, F.; Koppens, F. H. L. Hybrid Graphene-Quantum Dot Phototransistors with Ultrahigh Gain. *Nat. Nanotechnol.* **2012**, *7*, 363–368.
21. Roy, K.; Padmanabhan, M.; Goswami, S.; Sai, T.; Ramalingam, G.; Raghavan, S.; Ghosh, A. Graphene-MoS_2 Hybrid Structures for Multifunctional Photoresponsive Memory Devices. *Nat. nanotechnol* **2013**, *8*, 826–830.
22. Mueller, T.; Xia, F.; Avouris, P. Graphene Photodetectors for High-Speed Optical Communications. *Nat. Photonics* **2010**, *4*, 297–301.
23. Echtermeyer, T.; Britnell, L.; Jasnos, P.; Lombardo, A.; Gorbachev, R.; Grigorenko, A.; Geim, A.; Ferrari, A.; Novoselov, K. Strong Plasmonic Enhancement of Photovoltage in Graphene. *Nat. Commun.* **2011**, *2*, 458.
24. Liu, Y.; Cheng, R.; Liao, L.; Zhou, H.; Bai, J.; Liu, G.; Liu, L.; Huang, Y.; Duan, X. Plasmon Resonance Enhanced Multicolour Photodetection by Graphene. *Nat. Commun.* **2011**, *2*, 579–585.
25. Liu, C.; Chang, Y.; Norris, T. B.; Zhong, Z. Graphene Photodetectors with Ultra-Broadband and High Responsivity at Room Temperature. *Nat. Nanotechnol.* **2014**, *9*, 273–278.
26. Rossler, C.; Hof, K.-D.; Manus, S.; Ludwig, S.; Kotthaus, J. P.; Simon, J.; Holleitner, A. W.; Schuh, D.; Wegscheider, W. Optically Induced Transport Properties of Freely Suspended Semiconductor Submicron Channels. *Appl. Phys. Lett.* **2008**, *93*, 071107.
27. Sukhovatkin, V.; Hinds, S.; Brzozowski, L.; Sargent, E. H. Colloidal Quantum-Dot Photodetectors Exploiting Multiexciton Generation. *Science* **2009**, *324*, 1542–1544.
28. George, P. A.; Strait, J.; Dawlaty, J.; Shivaraman, S.; Chandrashekhar, M.; Rana, F.; Spencer, M. G. Ultrafast Optical-Pump Terahertz-Probe Spectroscopy of the Carrier Relaxation and Recombination Dynamics in Epitaxial Graphene. *Nano Lett.* **2008**, *8*, 4248–4251.
29. Sinha, D.; Lee, J. U. Ideal Graphene/Silicon Schottky Junction Diodes. *Nano Lett.* **2014**, *14*, 4660–4664.
30. Chelikowsky, J. R.; Cohen, M. L. Electronic Structure of Silicon. *Phys. Rev. B* **1974**, *10*, 5095–5107.
31. Li, X.; Magnuson, C. W.; Venugopal, A.; An, J.; Suk, J. W.; Han, B.; Borysiak, M.; Cai, W.; Velamakanni, A.; Zhu, Y.; *et al.* Graphene Films with Large Domain Size by a Two-Step Chemical Vapor Deposition Process. *Nano Lett.* **2010**, *10*, 4328–4334.
32. Li, X.; Magnuson, C. W.; Venugopal, A.; Tromp, R. M.; Hannon, J. B.; Vogel, E. M.; Colombo, L.; Ruoff, R. S. Large-Area Graphene Single Crystals Grown by Low-Pressure Chemical Vapor Deposition of Methane on Copper. *J. Am. Chem. Soc.* **2011**, *133*, 2816–2819.
33. Biswas, C.; Günes, F.; Loc, D. D.; Lim, S. C.; Jeong, M. S.; Pribat, D.; Lee, Y. H. Negative and Positive Persistent Photoconductance in Graphene. *Nano Lett.* **2011**, *11*, 4682–4687.